Electronic Supplementary Information

Structure and Oxygen vacancy engineered CuCo-layered double oxides nanotube arrays as advanced bifunctional electrocatalysts for overall water splitting

Zifeng Zeng[1], Zhifeng Gao[1], Zicheng Guo[1], Xiaowei Xu[1, 2], Yian Chen[3], Ying Li[1*], Dandan Wu[1*], Lin Lin[4*], Runping Jia[1], Sheng Han[4]*

[1]School of Materials Science and Engineering, Shanghai Institute of Technology, Shanghai, 201418, PR China, xiaoweixu@sit.edu.cn

[2]State Key Laboratory of Polymer Materials Engineering, Chengdu 610065, PR China

[3]Shanghai Fengxian High School, Shanghai, 201400, PR China

[4]School of Chemical and Environmental Engineering, Shanghai Institute of Technology, Shanghai, 201418, PR China

Email: xiaoweixu@sit.edu.cn; liying86@sit.edu.cn; wdan1008@163.com; linlin@sit.edu.cn

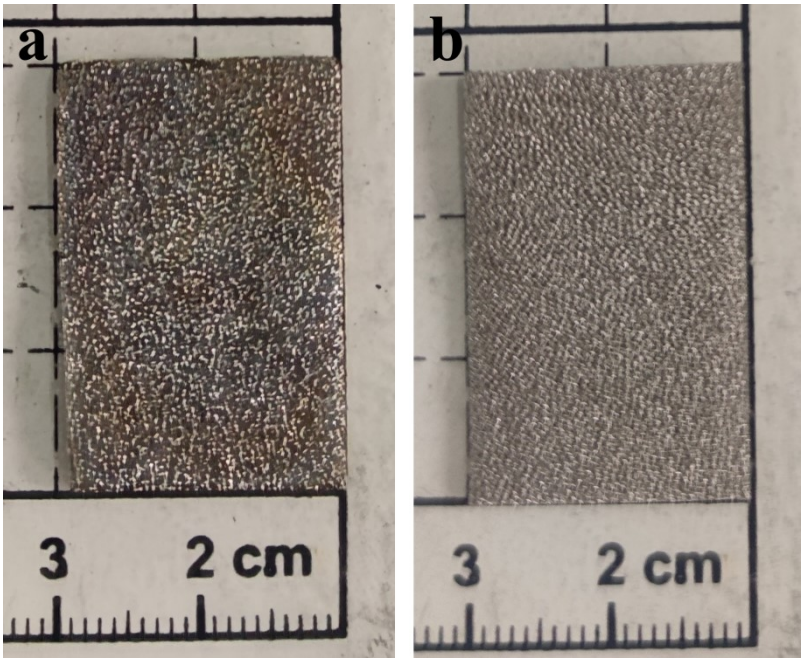

Figure S1. Photograph of NF a) before and b) after cleaning.

The bare NF (2 cm × 3 cm) was immersed in 3 M HCl for 10 min by ultrasonic treatment to remove the surface oxide layer, then washed with ethanol and DI water three times. Finally, the NF was air-dried and reserved.

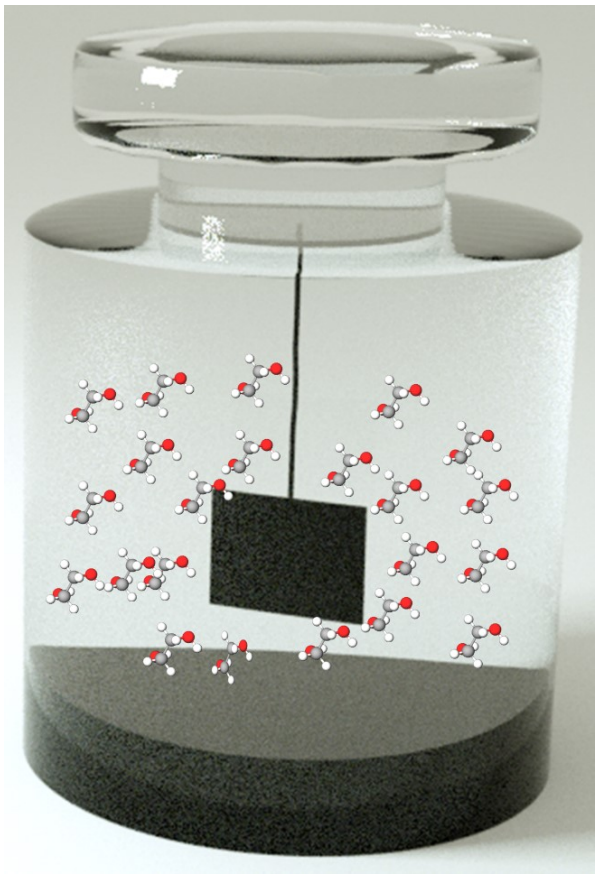

Figure S2. Schematic diagram of ethylene glycol gas phase reduction.

First, a NF coated with CuCo-LDO HNTAs was suspended in a wide bottle containing ethylene glycol (Figure S2, Supporting Information), which was sealed and placed in an oven. Second, when the temperature reached 200 °C, the ethylene glycol solution volatilized into gas, which filled the whole bottle. Finally, the ethylene glycol steam reacted with the CuCo-LDO HNTAs, leaving the outer topologically transformed to O-vacancy-rich CuCo-LDO HNTAs. Accordingly, the mechanism of this gas phase reduction process could be described via the following equations:

$$CuCo\text{-}LDO\ (s) + C_2H_6O_2\ (g) \rightarrow O_v\text{-}CuCo\text{-}LDO + C_2H_2O_2\ (g) + H_2O_2\ (g)$$

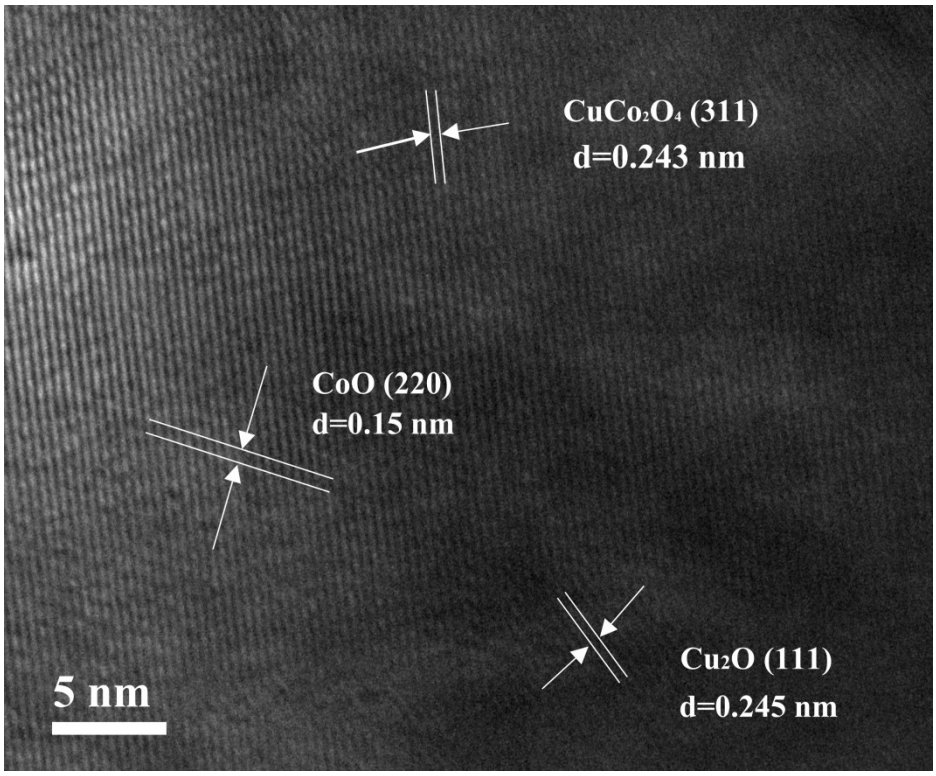

Figure S3. HRTEM image of CuCo-LDO.

The HRTEM image CuCo-LDO reveal the lattice fringes of the $CuCo_2O_4$ (311) plane with a spacing of 0.243 nm, the CoO (220) plane with a spacing of 0.15 nm, as well as the (111) plane of CuO_2 with a spacing of 0.245 nm.

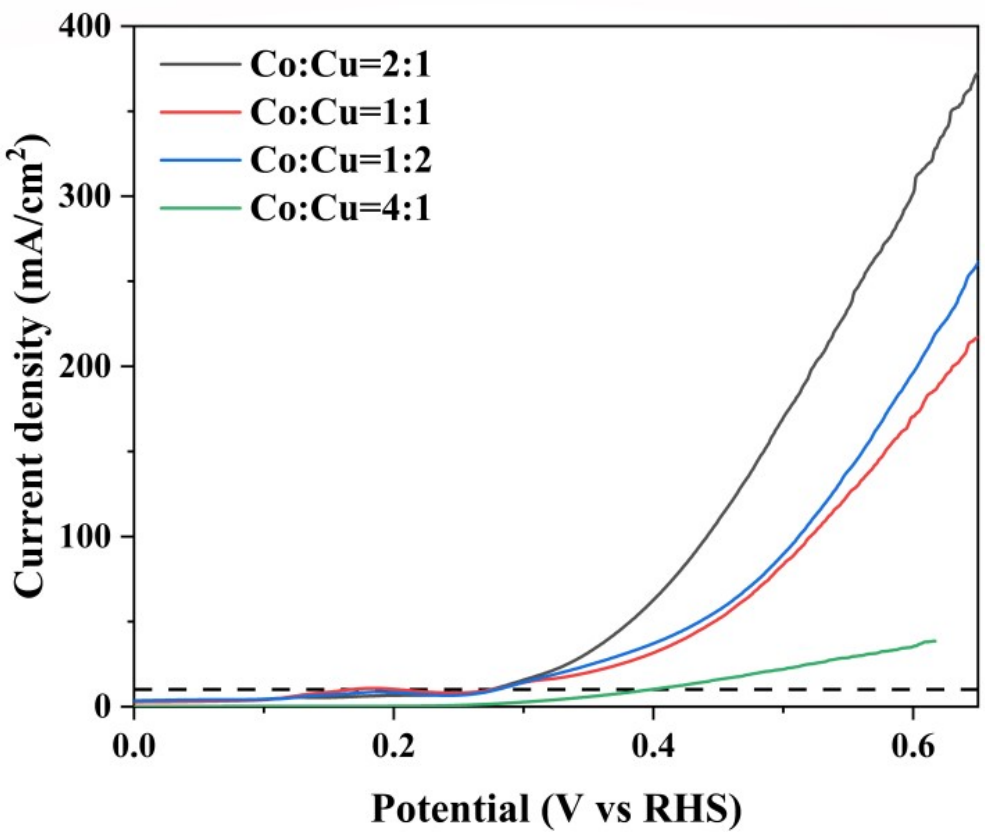

Figure S4. OER performances of CuCo-LDH with different Co-Cu ratios.

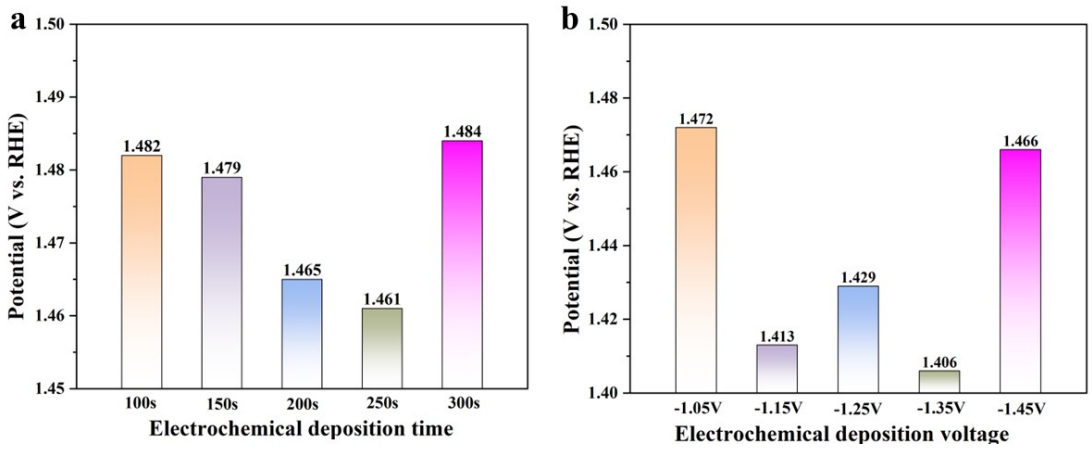

Figure S5. OER performance of CuCo-LDH under different electrochemical deposition conditions at 10 mA·cm^{-2}: a) time; b) voltage.

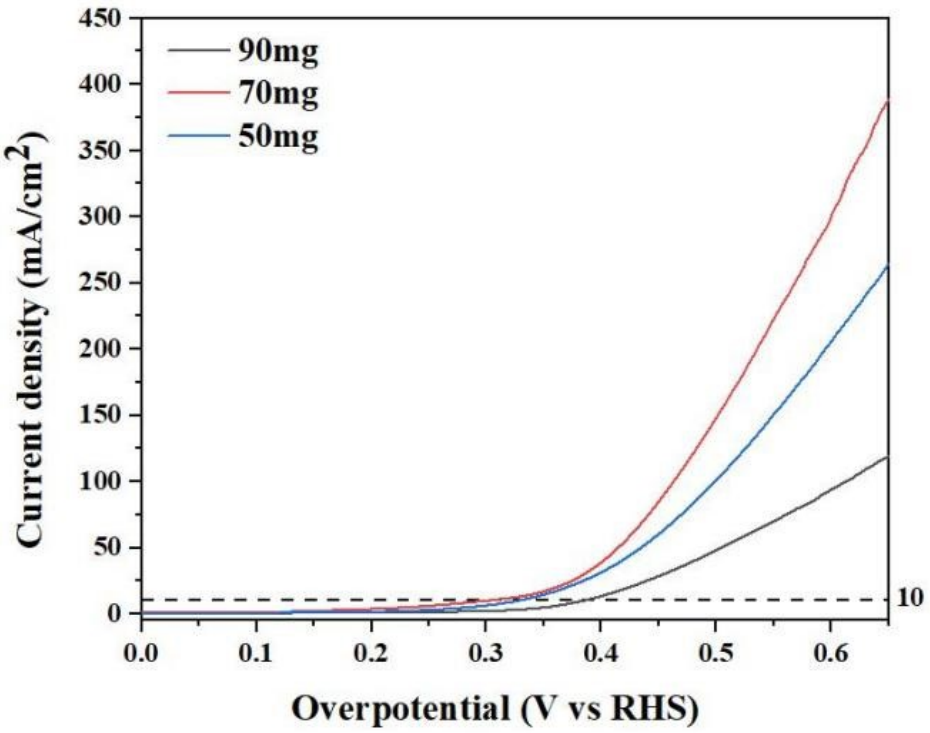

Figure S6. OER performances of MOF-CuCo-LDH HNTAs with different organic ligand content.

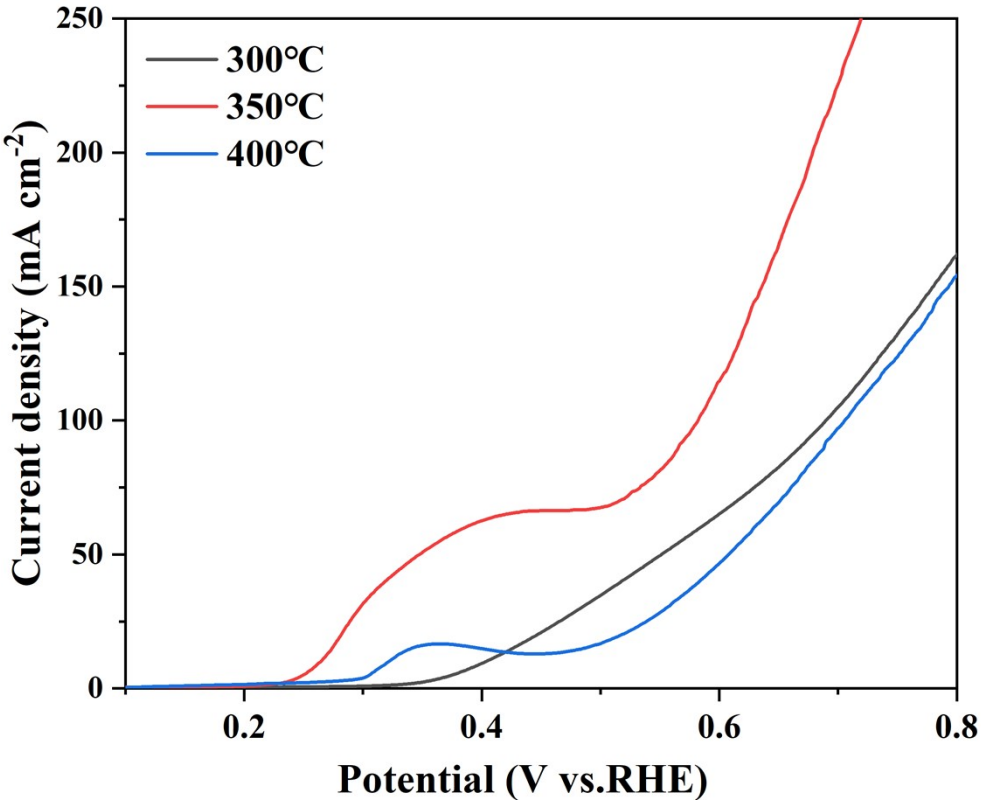

Figure S7. OER performances of CuCo-LDH HNTAs with different annealing temperatures.

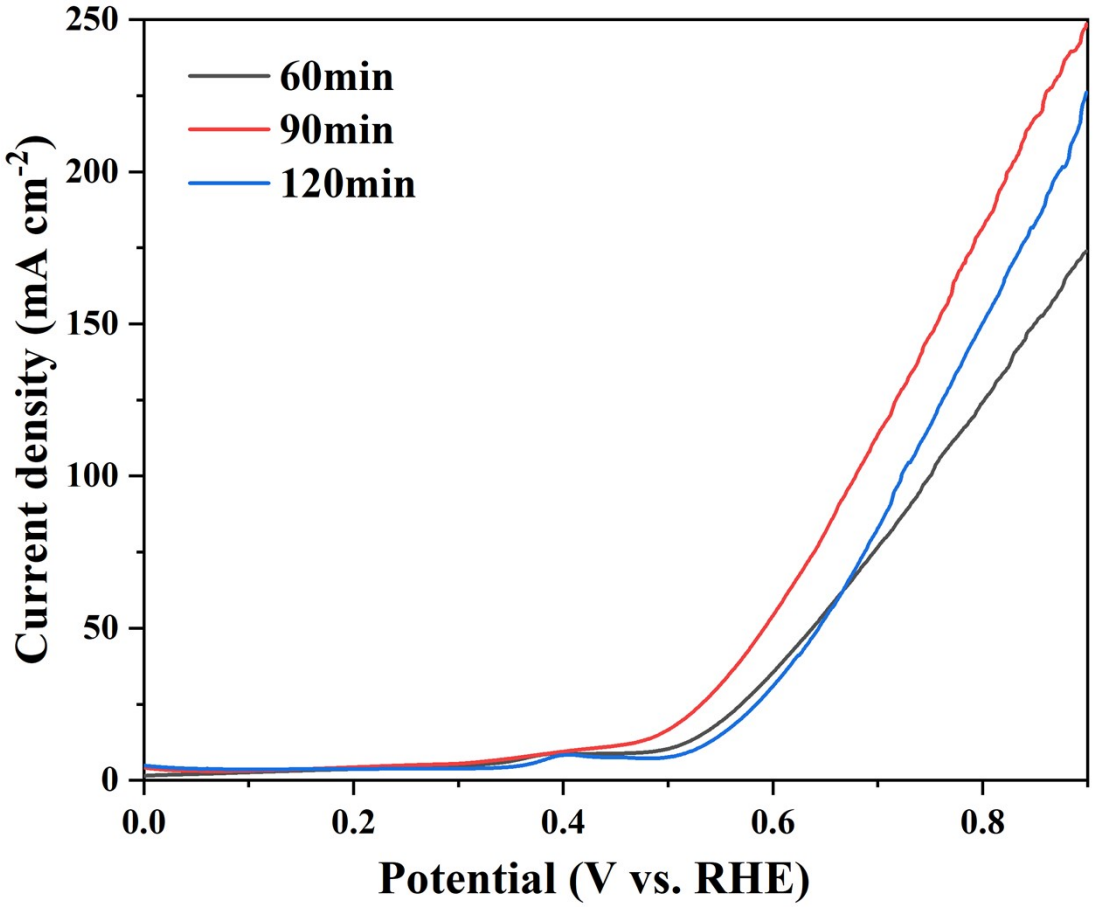

Figure S8. OER performances of O_v-CuCo-LDO HNTAs with different annealing time.

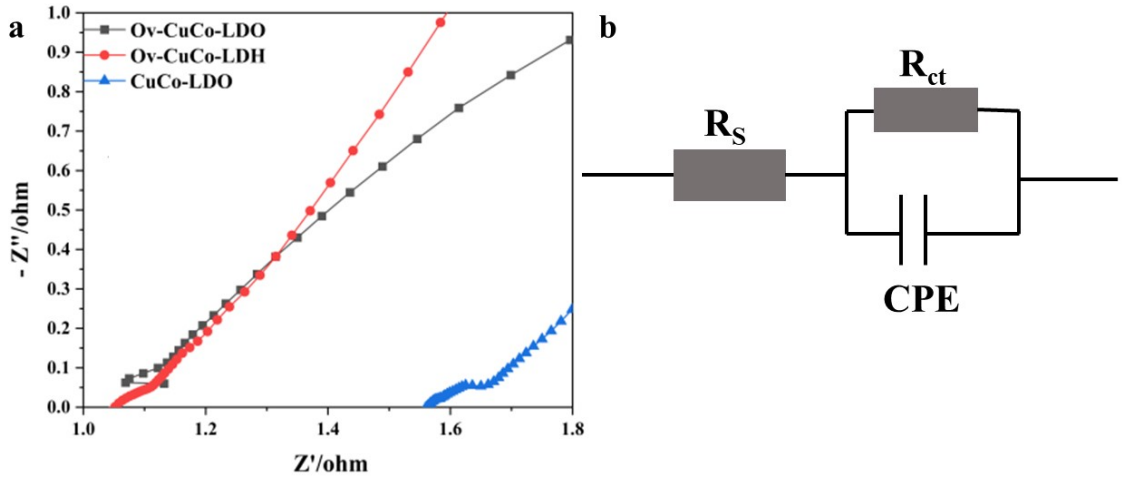

Figure S9. a) Impedance diagrams of, O_v-CuCo-LHD and CuC0-LDO for OER; b) the equivalent circuit of O_v-CuCo-LDO HNTAs.

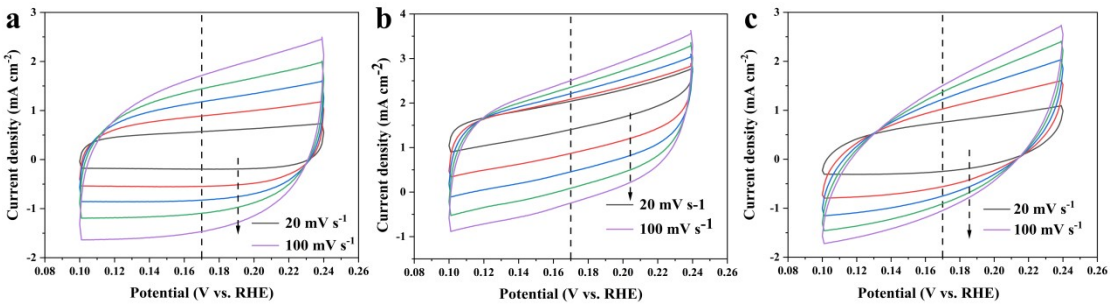

Figure S10. Cyclic voltammograms of a) O_v-CuCo-LDO, b) CuCo-LDO, and c) CuCo-LDH in the non-faradaic capacitance current range.

The non-faradaic capacitance (C_{dl}) is the key index for detecting the ECSA. CV curves of O_v-CuCo-LDO, CuCo-LDH, and CuCo-LDO catalysts under different scan rates in a non-Faradaic region of 0.10 to 0.24 V (vs. RHE) are shown in Figure S10. The electrochemical double layer capacitance（C_{dl}）is estimated by plotting the charging current differences $\Delta j = (j_a - j_c)/2$ at the applied potential of 0.17 V (vs. RHE) against different scan rates from 20, 40, 60, 80, and 100 $mV \cdot s^{-1}$, in which the slope of the linear is fitted twice of C_{dl}. C_{dl} values are 66, 59, and 56 $mF \cdot cm^{-2}$ for O_v-CuCo-LDO, CuCo-LDH, and CuCo-LDO catalysts, respectively.

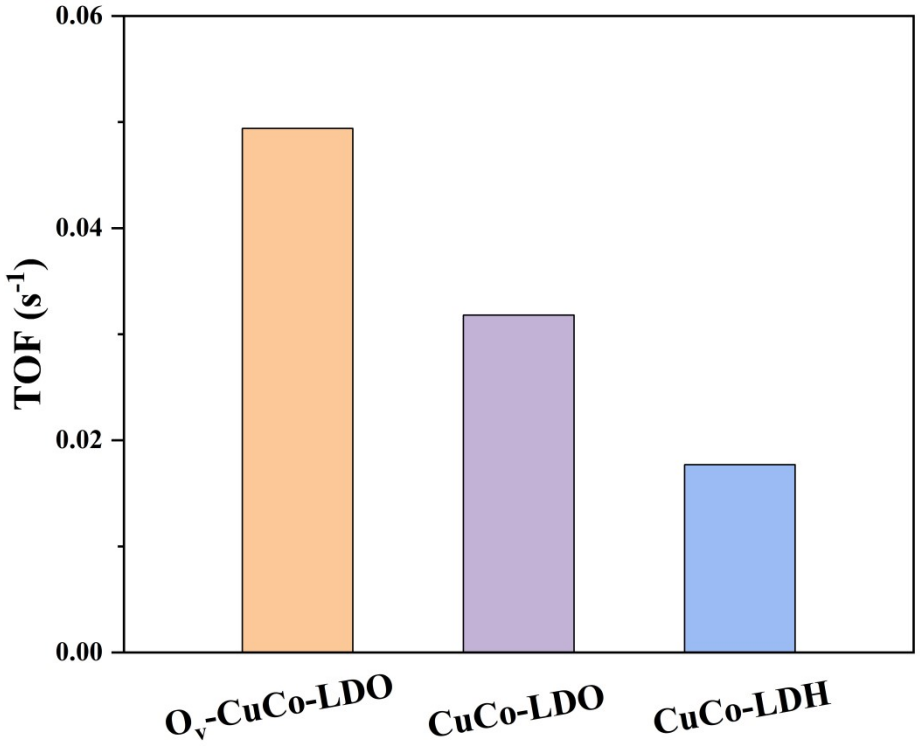

Figure S11. The TOF value of O_v-CuCo-LDO, CuCo-LDO, and CuCo-LDH at an overpotential of 72.5 mV.

Calculation of turnover frequency (TOF): Assuming that every metal atom is involved in the OER electrocatalysis. The TOF value of different catalysts were estimated according to the following formula:

$$TOF = \frac{J \times A}{n \times F \times m}$$

Wherein, J ($mA \cdot cm^{-2}$) is the current density at a given overpotential (e.g. η=72.5 mV), A is the surface area of the electrode (1*1 cm^2 for O_v-CuCo-LDO), F is the Faraday constant (96485.3 $C \cdot mol^{-1}$), m is the number of moles of metal on the electrode, and n is the electron transfer number (4 for OER).

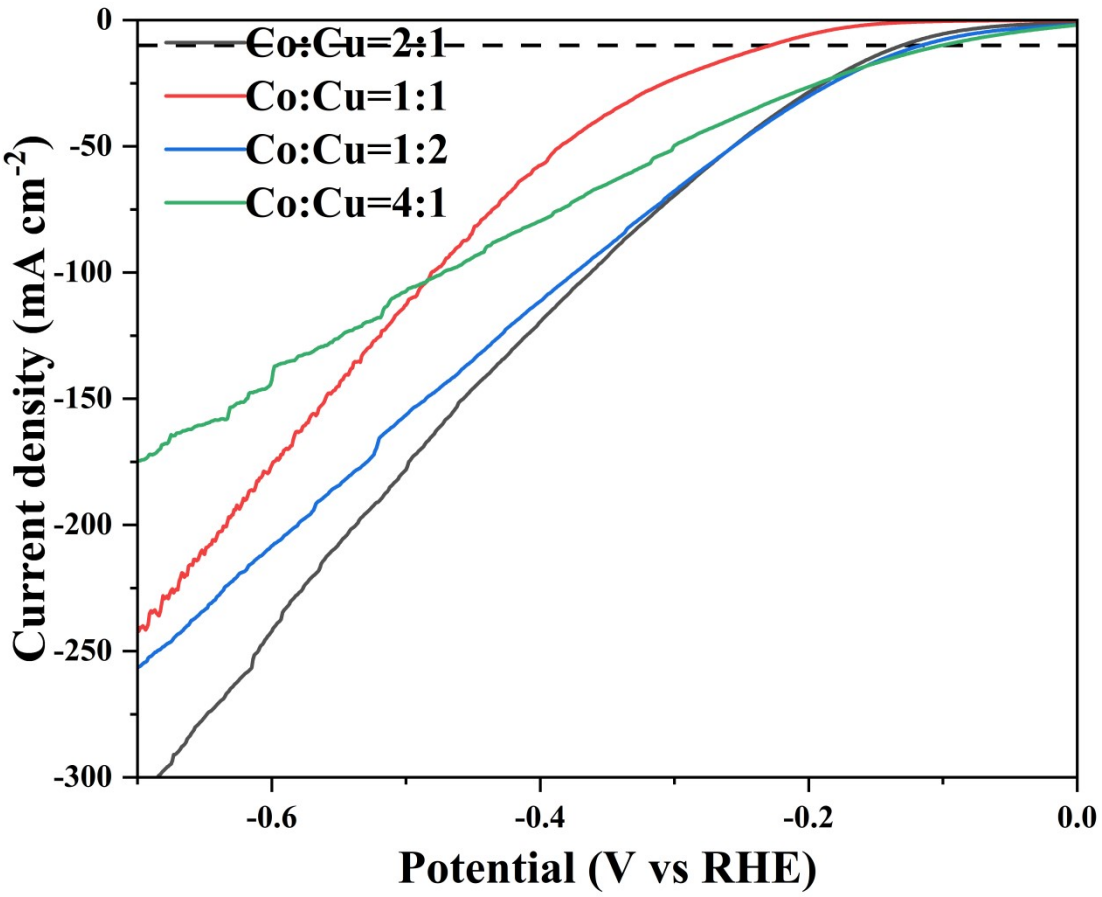

Figure S12. HER performances of CuCo-LDH with different Co-Cu ratios.

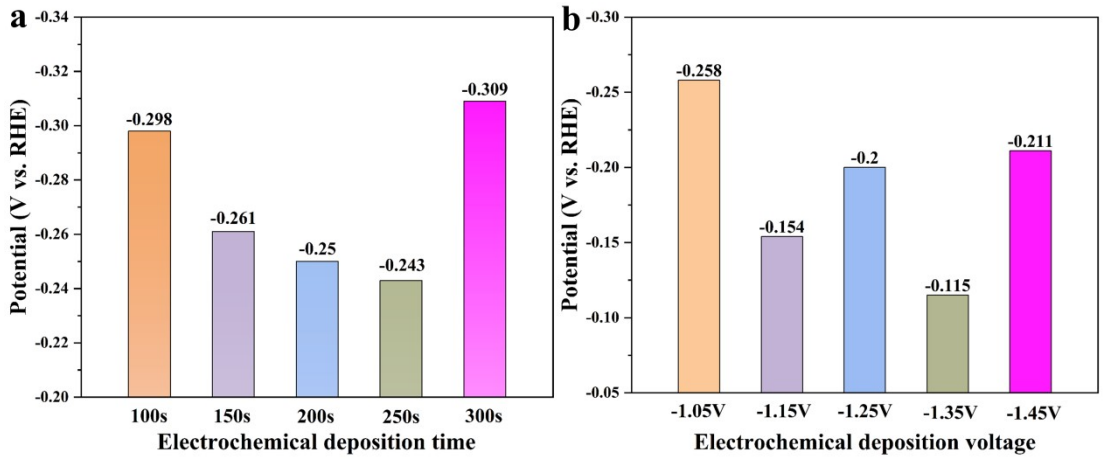

Figure S13. HER performance of CuCo-LDH under different electrochemical deposition conditions at 10 mA·cm^{-2}: a) time; b) voltage.

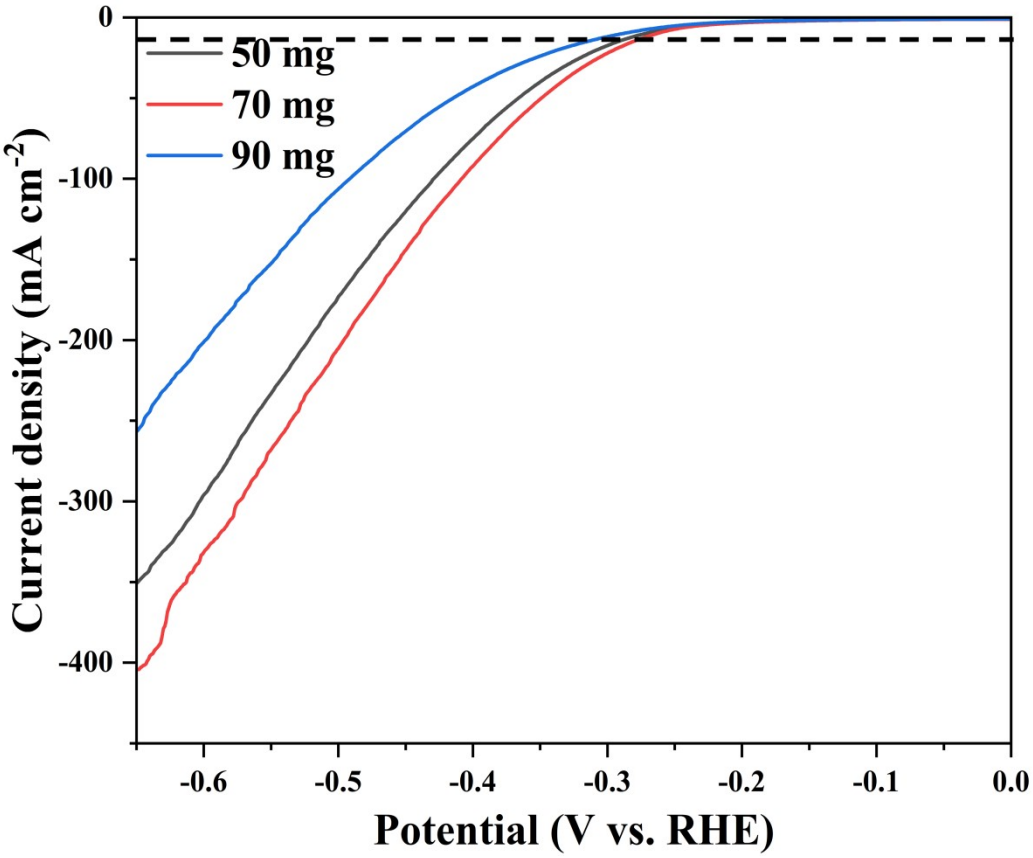

Figure S14. HER performances of MOF-CuCo-LDH HNTAs with different organic ligand content.

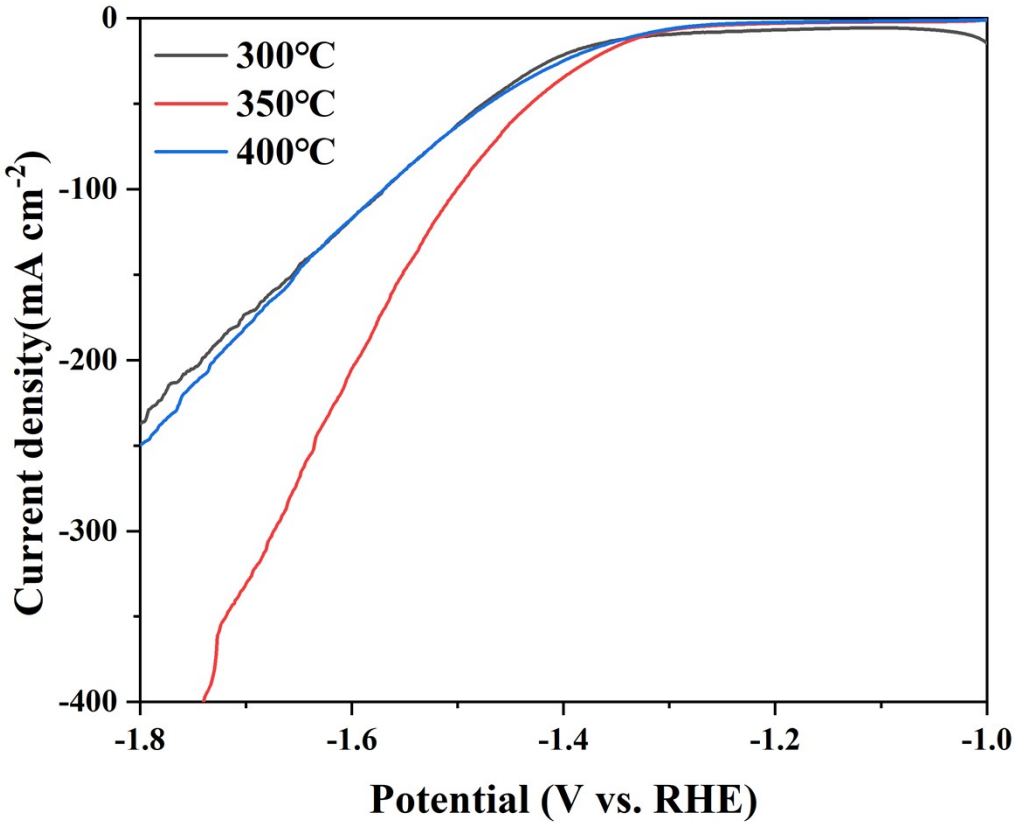

Figure S15. HER performances of CuCo-LDO HNTAs with different annealing temperatures.

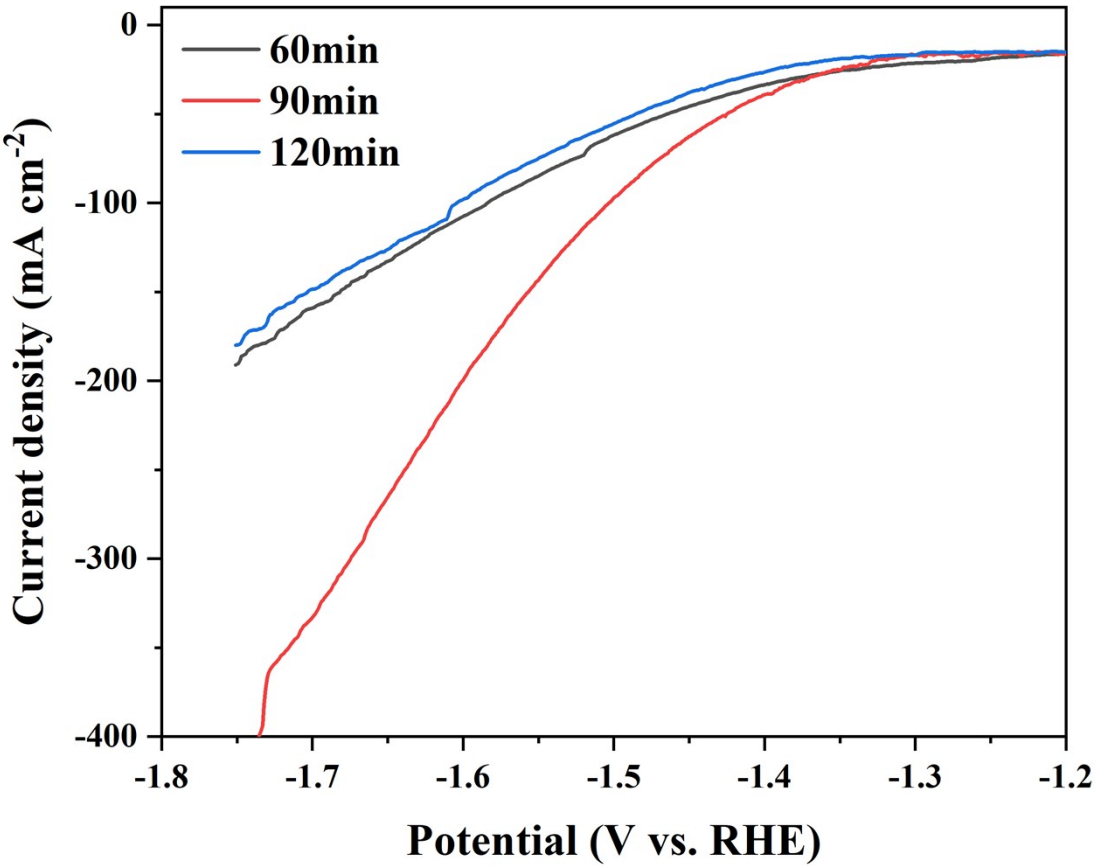

Figure S16. HER performances of O_v-CuCo-LDO HNTAs with different annealing time.

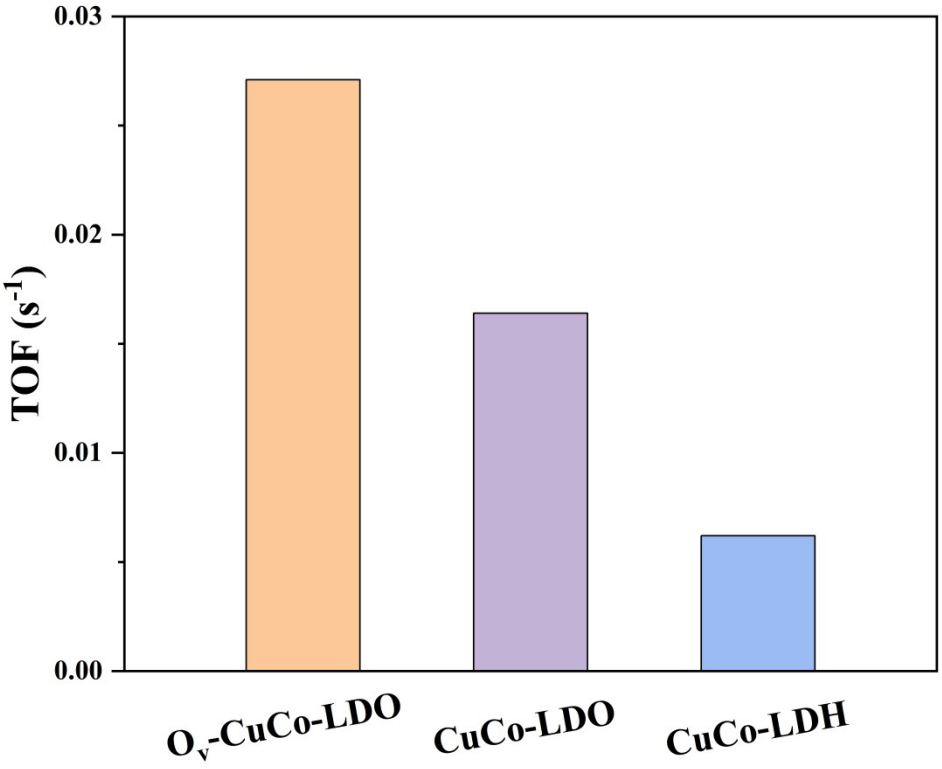

Figure S17. The TOF absolute value of O_v-CuCo-LDO, CuCo-LDO, and CuCo-LDH at an overpotential of -53.9 mV.

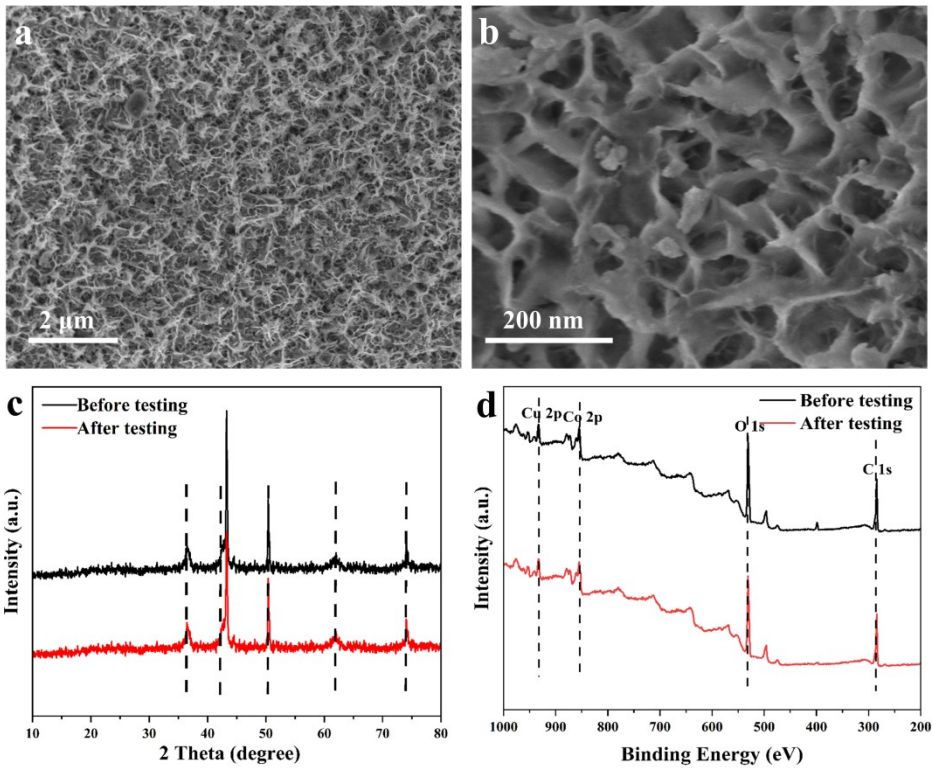

Figure S18. SEM images of O_v-CuCo-LDO after 20 h cycling (a, b), XRD pattern (c), and XPS survey spectrum (d) of O_v-CuCo-LDO before and after 20 h cycling.

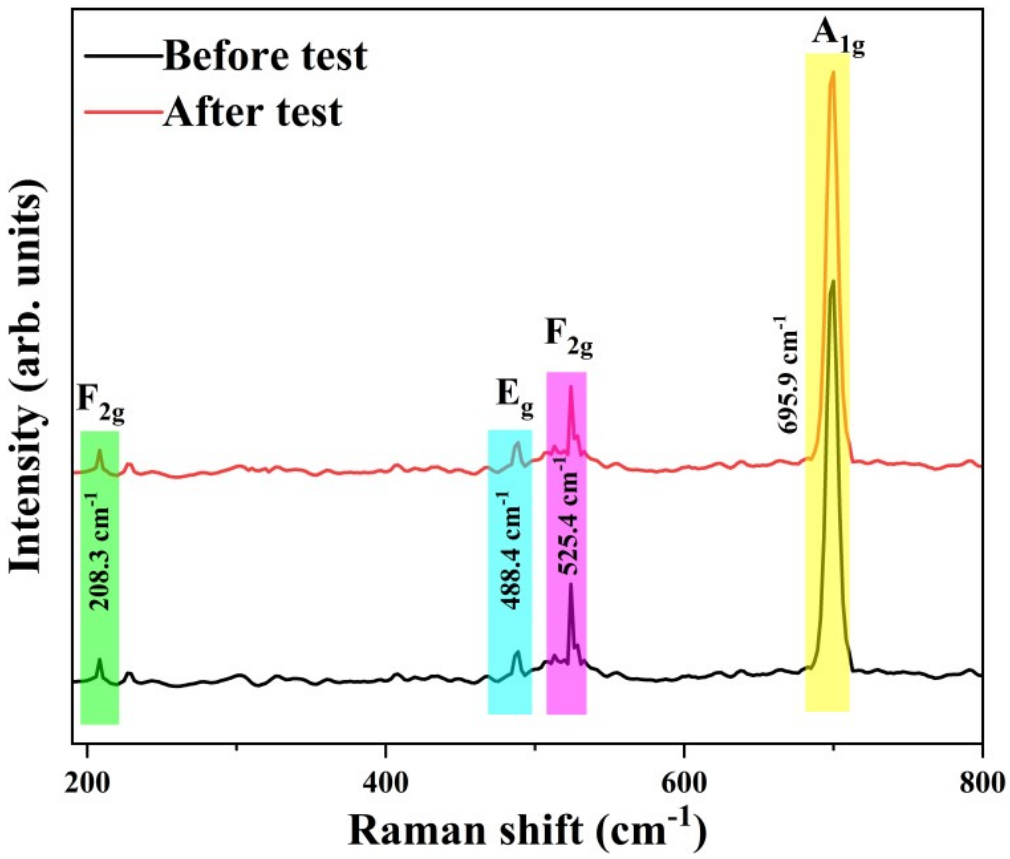

Figure S19. Raman spectra of O_v-CuCo-LDO before and after the continuous electrocatalysis.

Figure S20. Photograph of the gas collection device and the amount of hydrogen and oxygen gas generated at 0 min, 20min, and 60min.

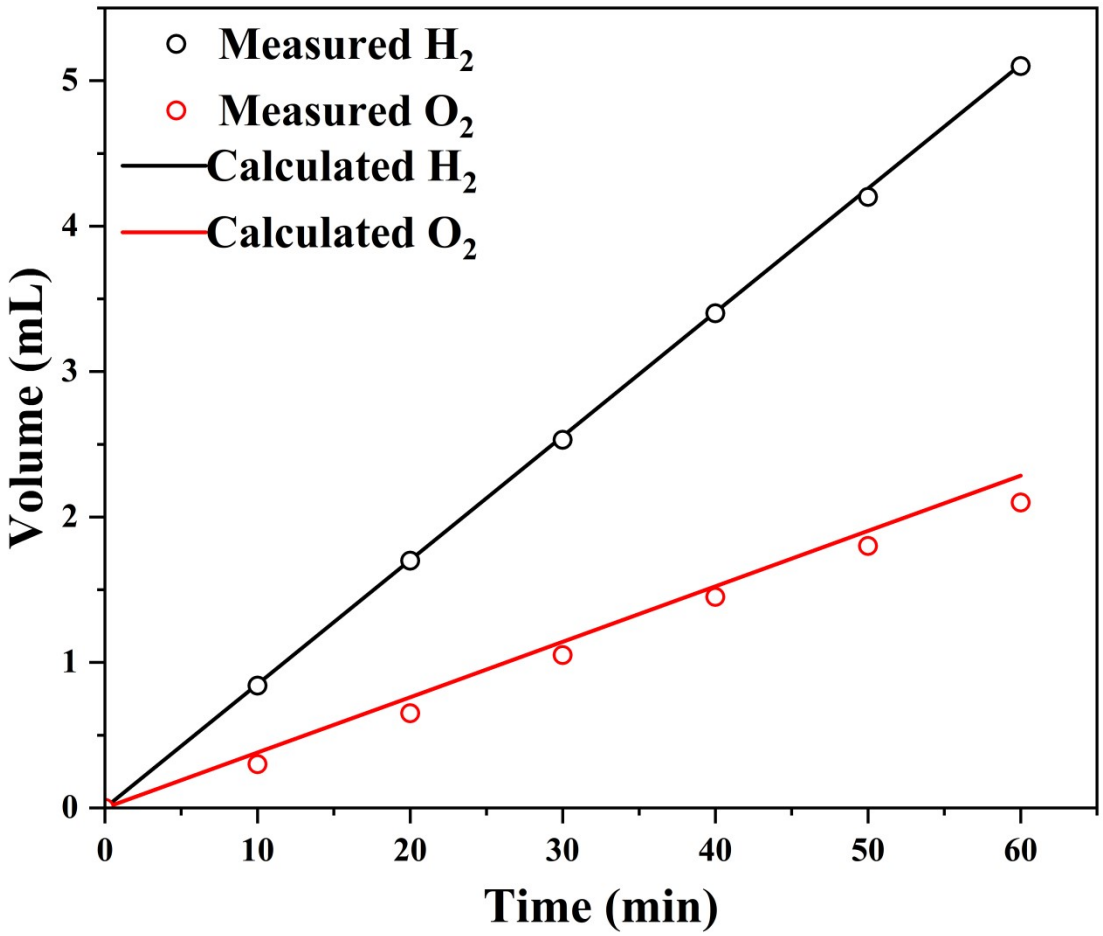

Figure S21. Experimental H_2 and O_2 production over time versus theoretical quantities assuming a ~98% Faradaic efficiency for HER and OER in 1.0 M KOH at 10 $mA \cdot cm^{-2}$.

Table S1. Comparative electrochemical OER performances of different electrocatalytic materials in alkaline medium

Catalysts	Electrolyte	Overpotential (mV) @ 10 mA·cm^{-2}	Ref.
O_v-CuCo-LDO	1.0 M KOH	72.5	This work
Ru@NiCo-MOF HPNs		284	[1]
$Cu_{1-x}Co_{2+x}O_4$ nanoflakes		267	[2]
CuCoS/CC		276	[3]
CoFeO@BP		266	[4]
$Co_3Mo/CoMoO_x$		256	[5]
Mn-CoP		288	[6]
Ni-Fe LDH@NiCu		218	[7]
Fe-S-$NiMoO_4/MoO_3$		212	[8]

References:

[1]. Liu, D., et al., 3D Porous Ru-Doped NiCo-MOF Hollow Nanospheres for Boosting Oxygen Evolution Reaction Electrocatalysis. Inorganic Chemistry, 2021. 60(8): p. 5882-5889.

[2]. Yang, H., et al., Non-metallic electronic regulation in CuCo oxy-/thio-spinel as advanced oxygen evolution electrocatalysts. Science China Chemistry, 2021. 64(1): p. 101-108.

[3]. Luo, H., et al., Engineering Ternary Copper-Cobalt Sulfide Nanosheets as High-performance Electrocatalysts toward Oxygen Evolution Reaction. Catalysts, 2019. 9(5): p. 459.

[4]. Xingyun Li, L.X.L.Z., Adaptive Bifunctional Electrocatalyst of Amorphous CoFe Oxide @ 2D Black Phosphorus for Overall Water Splitting. Angewandte Chemie International Edition, 2020. 47(59): p. 21106-21113.

[5]. Liu, Y., et al., Interfacing Co_3Mo with $CoMoO_x$ for synergistically boosting electrocatalytic hydrogen and oxygen evolution reactions. Chemical Engineering Journal, 2022. 431: p. 133240.

[6]. Liu, Y., et al., Porous Mn-doped cobalt phosphide nanosheets as highly active electrocatalysts for oxygen evolution reaction. Chemical Engineering Journal, 2021. 425: p. 131642.

[7]. Zhou, Y., et al., Exceptional Performance of Hierarchical Ni-Fe (hydr)oxide@NiCu Electrocatalysts for Water Splitting. Advanced Materials, 2019. 31(8): p. 1806769.

[8]. Zhang, Y., et al., MoO_3 crystal facets modulation by doping heteroatom Fe from polyoxometalate for quasi-industrial oxygen evolution reaction. Applied Catalysis B: Environmental, 2021. 298: p. 120582.